A 2.3 to 25 keV XAS beamline at LNLS

H. C. N. Tolentino,[a] A. Y. Ramos,[a,b]* M. C. M. Alves,[a] R. A. Barrea,[a,c] E. Tamura,[a] J. C. Cezar[a,d] and N. Watanabe[a,e]

[a]LNLS CP6192 CEP13083-970 Campinas/SP, Brazil, [b]LMCP UMR7590 Paris, France, [c]Universidad Nacional de Córdoba, FaMAF, Argentina, [d]IFGW UNICAMP Campinas, Brazil, and [e]Instituto de Química, UNICAMP Campinas, Brazil. E-mail: aramos@lnls.br

The LNLS XAS beamline has been operating for external users since July 1997. Many facilities and improvements have been progressively added to it, extending the range of applications. Here, a technical description of the main beamline components is given, and results concerning important points, such as available flux at low and high energies, harmonic contamination, energy resolution and stability, are presented. Some key results are given to demonstrate the beamline performance and limitations. It is shown that the beamline can cover a large energy range, starting from the rather low energy of 2.3 keV up to 25 keV.

Keywords: XAS; beamlines; energy resolution; harmonic content.

1. Introduction

The LNLS (Laboratório Nacional de Luz Síncrotron, Campinas, Brazil) synchrotron light source is a third-generation storage ring with a natural emittance of 100 nm rad and a critical energy of 2.08 keV. The facility is composed of a 1.37 GeV electron storage ring and a linear accelerator that injects into the ring at 120 MeV (Rodrigues *et al.*, 1998). The maximum stored current attained up to now is 170 mA at 1.37 GeV and the average lifetime is 15 h at 150 mA. Inside the storage ring, the LNLS group is currently assembling a 500 MeV synchrotron booster in order to increase the injection energy into the ring and improve the stored beam performance (Liu Lin *et al.*, 1999). A significant increase in the stored electron beam current and a better control during injection and ramp-up procedures are expected.

The synchrotron light source was opened to external users in July 1997 and, nowadays, the facility has nine operative beamlines installed in bending-magnet ports (Craievich & Rodrigues, 1998; Rodrigues *et al.*, 1998). The basic components of the X-ray absorption spectroscopy (XAS) beamline were installed and commissioned during the second semester of 1996 and the first semester of 1997. The beamline has been open to the users community since July 1997 (Tolentino *et al.*, 1998). Many facilities and improvements have been progressively added, which has widened the range of experimental possibilities. We present here the general beamline components, some experimental facilities and important commissioning results.

The beamline optics is designed to cover the X-ray range from 2.3 keV up to 25 keV using two different channel-cut crystals. This beamline is the hard X-ray complement of the LNLS soft X-ray spectroscopy (SXS) beamline that covers the range from 800 eV up to about 4 keV. In this beamline, the Au-coated toroidal mirror imposes limitations on XAS measurements around the 2.2 to 2.5 keV region due to Au $M_{4,5}$ absorption edges (Abbate *et al.*, 1999). Unlike on the SXS beamline, there is no mirror or focusing element installed on the XAS beamline. Even without any optics to reject harmonics, experimental data show that harmonic contamination can be made to be negligible over the whole energy range by adequate choices of the experimental conditions. Special attention is paid to the lowest attainable energies, the sulfur *K*-edge. The energy resolution and stability, closely related to the storage-ring performance, have been well characterized and their ultimate performances are discussed. Finally, we describe the experimental facilities available, as well as new developments concerning sample environment and detection. The number of facilities and the understanding of the beamline performances in some extreme cases have extended the range of applications and improved data quality.

2. Beamline description

2.1. *General description*

The layout and main components of the LNLS XAS beamline are shown in Fig. 1. At the exit of the photon source (*a*), and inside the shield wall, the front-end (*b*) is devoted to radiation protection and vacuum safety. The first slit system (*c*) is located at 10.4 m from the source, just before the monochromator (*d*), and defines the lateral and vertical dimensions of the polychromatic beam impinging on the

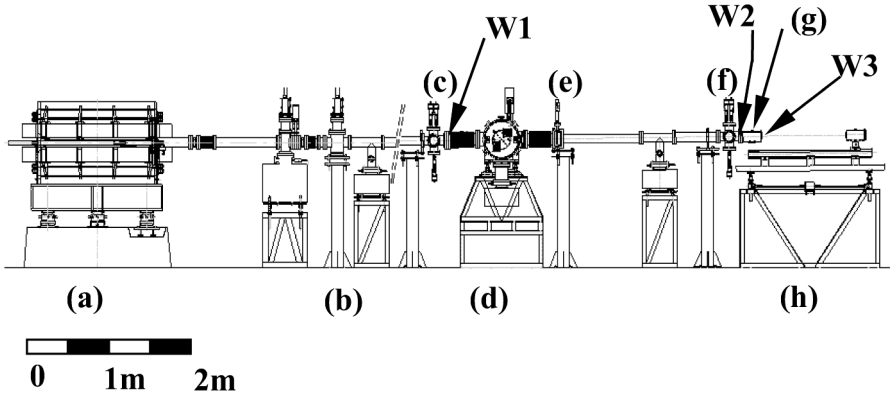

Figure 1
Layout and main components of the beamline: (*a*) the bending-magnet source, (*b*) the front-end, (*c*) the pre-monochromator UHV slits, (*d*) the monochromator, (*e*) the post-monochromator shutter, (*f*) the post-monochromator UHV slits, (*g*) the ion chamber, (*h*) the workstation. Three windows are located along the beamline: the pre-monochromator Be window (*W*1), the post-monochromator Be window (*W*2), the end-line polymeric window (*W*3).

monochromator. After the monochromatic shutter (*e*) and close to the end of the beamline, the post-monochromator slit system (*f*) is devoted to eliminating undesirable background radiation, due to scattering and additional reflections from the monochromator. An ion-chamber detector (*g*), attached to the end of the beamline, monitors the beam flux delivered to the experimental station (*h*). Three windows (*W*1, *W*2, *W*3) are inserted into the beam from the source to the experimental station.

2.2. *Photon source*

The XAS beamline is installed in the 15° exit port of the DB04 bending magnet. The vertical divergence of the source at the critical energy (2.08 keV) is dominated by the intrinsic radiation opening angle $1/\gamma$ (γ is the relativistic factor) and is around $\sigma_{y'} = 0.385$ mrad. Until November 1999, a large vertical beam mode operation, with a vertical coupling of 3%, had been used, giving a vertical source size (FWHM) of $s_y = 522$ µm. Since then, the horizontal and vertical dimensions (FWHM) of the source, under normal vertical coupling operation of 0.3% (Lira *et al.*, 1998), are $s_x = 750$ µm and $s_y = 168$ µm, respectively.

The maximum horizontal acceptance, defined by the mask in the front-end, is 8 mrad. The lateral size of the monochromator crystals, 15 mm for channel-cut crystals at about 11.3 m, limits this acceptance to about 1.3 mrad. In fact, the ultimate limitation is imposed by the sample environment to less than 1 mrad, at about 14.5 m from the source. The integrated power per horizontal divergence is 1.8 W mradH^{-1} at a nominal current of 100 mA.

The orbit measurement and correction system of the LNLS synchrotron light source has been recently upgraded, with the addition of 12 new vertical correctors, new beam-position-monitor electronics modules and changes to the orbit control software. These changes have allowed a performance of ±3 µm in the vertical beam position repeatability between shifts and of ±5 µm in the orbit fluctuations inside the vacuum chamber during a users shift (Franco *et al.*, 1999).

2.3. *Front-end*

The main components of the front-end are the water-cooled photon mask, the water-cooled photon shutter, a gate valve, a fast-closing valve, a gamma-ray shutter and a fast vacuum sensor (Abbate *et al.*, 1999). Devoted mainly to vacuum safety, the fast valve can close, in case of an accident, in less than 20 ms. The gamma-ray shutter is kept closed only during the injection. The photon shutter is interlocked to the vacuum of the monochromator and it is maintained open under normal operation to ensure thermal stabilization of the crystal monochromator.

2.4. *Slit systems*

The two UHV slit systems are based on four independent mechanical feedthroughs, each one supporting at its ends a Ta blade mounted on a copper block. Each horizontal Ta blade is mounted in a 2 inch-stroke feedthrough and can withstand most of the radiation power on the slit system. Each vertical blade is mounted in a 1 inch-stroke feedthrough and is almost completely hidden from the beam by the horizontal blades. All motions are controlled by step-motors, and translations have a resolution of 1.6 µm step^{-1}. Within the 8 mrad accepted by the photon mask, there is a total power of 15 W (1.8 W mradH^{-1}). The copper blocks help to dissipate the radiation power on the blades with no need for additional cooling, due to the low power from the bending magnet.

2.5. *Monochromator*

The angular position of the monochromator is achieved by a single high-precision translation. The translation stage, with a resolution of 0.5 µm per step, is connected to a 200 mm-diameter drum by a thin steel wire and produces an angular resolution of 5 µrad step^{-1}, just enough for the required XAS experiments. This goniometer can cover the range from 0 to 90°. The covered energy range will depend on the crystal geometry and the mechanical mounting. The monochromator chamber can accept three different mountings: channel-cut crystal, double-crystal and high-resolution four-crystal monochromator mountings (Tolentino *et al.*, 1995). They were installed and tested during the initial commissioning of the beamline, but only the channel-cut crystal mounting has been used for experiments in the XAS beamline (Tolentino *et al.*, 1998).

The channel-cut crystal mounting supports two different crystals, selected by laterally sliding the chamber. The crystals currently installed in the monochromator chamber are Si(111) and Si(220). Both have a channel width, *h*, of 9.7 mm and their dimensions limit the angular range for the accessible Bragg angles from $\theta = 7°$ to $\theta = 56°$. The crystals and the available angular range define a covered energy range from 2.3 keV to 25 keV. As a consequence of the fixed separation of the two Bragg reflectors in the channel-cut crystal, the exit beam shifts vertically by $2h\cos\theta$ in relation to the incoming beam. Thence, when the Bragg angle scans from its maximum to minimum value, the vertical beam offset shifts from 10.8 to 19.2 mm relative to the white beam.

2.6. *Experimental station*

The experimental station is equipped with a granite table, supporting a 1.60 m-long rail aligned to the beam direction on which are mounted an *XY* remote-controlled sample holder, the detectors and experimental facilities. The granite table can withstand a maximum weight of 300 kg, and track the vertical position of the beam with an accuracy of 1 µm over a 120 mm stroke. In order to keep the beam spot at the same position on the sample, this track is performed automatically during an energy scan. In fact, the changes in beam offset are important only for rather low energies. For most applications, *e.g.* above 8 keV, the tracking is blocked.

XAS spectra can be collected either in transmission, electron or fluorescence modes. For usual transmission-mode experiments, three chambers are used. The first one is coupled to the beamline, the second is used for detecting the signal after the sample, and the third is used for measuring a reference sample or doubling the data set. For fluorescence yield detection, either a fast NaI scintillator detector or a solid-state Si(Li) detector is available. Electron detection is accomplished in the conversion electron yield (CEY) mode, based on an He-flow electron detector (Tourillon *et al.*, 1987).

Recently, a new multi-wire proportional counter (MWPC) gas detector has been developed (Barbosa *et al.*, 1998). The main features of the MWPC are the large active area (6 cm × 6 cm) and high counting-rate capability ($\sim 10^7$ counts s^{-1}) which allows fluorescence detection even with a high-intensity background beam. Comparison of XAS measurements using the Si(Li) detector and the MWPC as fluorescence detectors defined two domains of performance: the Si(Li) performs better for very diluted samples, but for intermediate samples the MWPC performs better (Barrea *et al.*, 2001).

The main experimental facilities available on the beamline include a closed-cycle He cryostat (10–300 K), a cryostat furnace (80–700 K) and a home-made furnace working under vacuum (300–1200 K). An electrochemical cell for *in situ* experiments has been developed to study the growth mechanism of thin metallic films and small aggre-

gates (Alves *et al.*, 2001). Two magnets are available for X-ray magnetic circular dichroism (XMCD) experiments, namely, a 0.9 T permanent magnet, that can flip mechanically in about 1 s, and a variable electromagnetic field in the range ±0.6 T, attained with a controllable power supply. The bores of both magnets are compatible with the closed-cycle He cryostat.

2.7. *Windows*

There are three windows along the beam path, from the source to the experimental station. They isolate the different vacuum conditions through the beamline and absorb part of the total radiation power, cutting the visible, infrared and ultraviolet light and limiting the flux at low X-ray energies. The first beryllium window (*W*1) isolates the UHV vacuum (10^{-10} to 10^{-11} mbar) of the storage ring and front-end from the vacuum of the monochromator chamber, maintained at a base pressure of 5×10^{-8} mbar. The second beryllium window (*W*2) isolates the beamline from the gas-filled ion chamber. Both beryllium windows have to withstand a pressure of 1 atm, to allow venting of the monochromator. An additional polymer (Mylar or Kapton) window (*W*3) separates the gas-filled ion chamber from the experimental station.

3. Flux throughput

The flux delivered by the bending magnet reaches its maximum value in the soft X-ray region. Owing to the absorption of the windows inserted into the beam path, the maximum of the flux distribution is shifted to higher energies (Fig. 2*a*). Before August 1999, the first, second and third windows were made out of 125 µm of beryllium, 300 µm of beryllium and 50 µm of Kapton, respectively. The maximum flux was around 5 keV and, in addition, harmonic contamination from the monochromator was greater than the fundamental reflection for energies below 3 keV (Tolentino *et al.*, 1998). In August 1999, the windows were substituted by two 25 µm-thick beryllium windows and a 6.3 µm-thick Mylar polymer window in order to shift the maximum flux distribution towards lower energies.

The theoretical predictions have been experimentally checked by measuring the photon flux as a function of the photon energy delivered by the Si(111) channel-cut crystal (Fig. 2*b*). The photon intensity was measured using a calibrated 100%-efficiency photodiode, placed just after the Mylar window. In this experiment, the pre-monochromator slits were set to 0.5 mm and 1.0 mm for the vertical and horizontal directions, respectively, giving an accepted angle of 0.05 mrad in the vertical and 0.1 mrad in the horizontal. The reported photon intensity was normalized for an electron beam current of 100 mA and an accepted horizontal divergence of 1 mrad. The experimental result is compared with the theoretical prediction, which was re-normalized by the Si(111) band-pass and the vertical acceptance. The low energies are more affected by the limited vertical accepted angle due to the increasing divergence of the beam when the energy decreases, shifting the maximum flux to around 4.5 keV. The coating of the Si photodiode has not been taken into account in the normalization process and should be responsible for the observed small deviation, especially evident at low energies, between the theoretical and the measured flux values. A gain of two orders of magnitude has been achieved at 2400 eV, making more than 10^{12} photons s^{-1} $mradH^{-1}$ (0.1% bandwidth)$^{-1}$ (100 mA)$^{-1}$ available at that energy. This improvement has extended the useful domain of the beamline down to energies as low as that of the sulfur *K*-edge.

The window replacement does not affect the available flux above 10 keV, the starting domain of the Si(220) crystal, up to 25 keV. In this range, the flux drops from 10^{11} to 10^{8} photons s^{-1} $mradH^{-1}$ (0.1% bandwidth)$^{-1}$ (100 mA)$^{-1}$. Even under such relatively low-flux conditions, the beamline has been used for XAS experiments at energies as high as that of the *K*-edges of Mo (20 keV) and Ru (22 keV).

4. Harmonic contamination

The harmonic contamination from the monochromator, *i.e.* contamination of the output beam with higher-order reflections (James, 1982), is one of the most common problems in absorption measurements. The output beam delivered by the silicon monochromator is given by $I_0 = I_{0f} + I_{0h}$, with I_{0f} and I_{0h} representing the fundamental and harmonic reflection intensities, respectively. The harmonic contamination can be expressed by the ratio $\alpha = I_{0h}/I_{0f}$. After the sample the intensity of the beam can be written in the same way, $I = I_f + I_h$, with $I_f = I_{0f}\exp(-\mu_f x)$ and $I_h = I_{0h}\exp(-\mu_h x) = \alpha I_{0f}\exp(-\mu_h x)$; x is the sample thickness; μ_f and μ_h are the linear

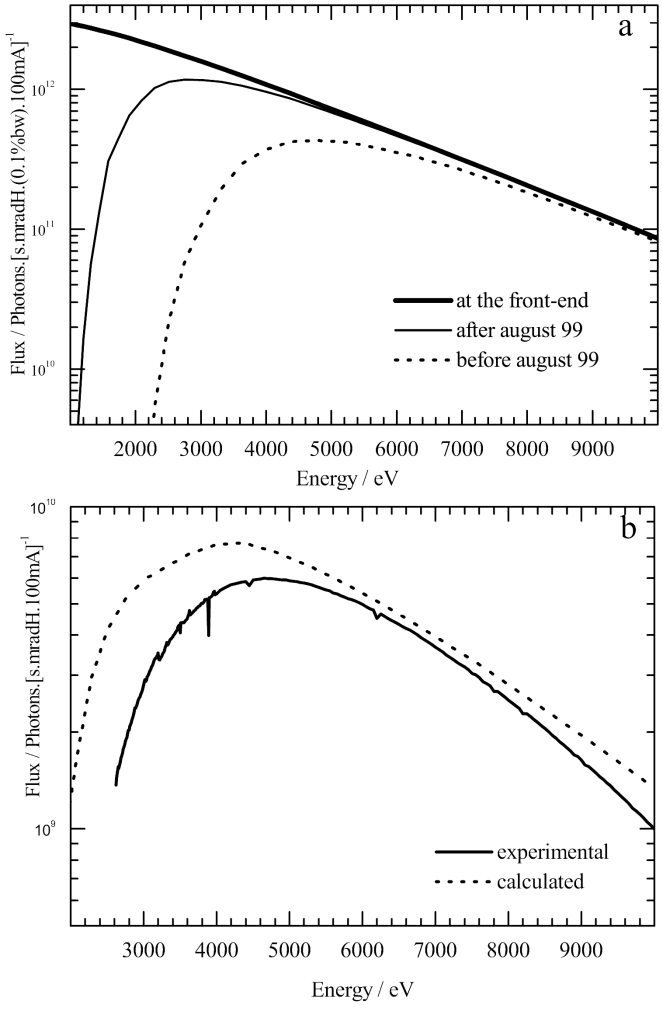

Figure 2
(*a*) Calculated photon flux at the end of the beamline, before and after windows substitution. (*b*) Photon intensity delivered by an Si(111) channel-cut crystal. The flux was measured using a 100% efficiency photodiode placed just after the window, at the end-station, and compared with the calculated one.

absorption coefficients of the sample for the energy of the fundamental beam and of the harmonic beam, respectively.

The measured absorption coefficient is affected in a non-linear way by the harmonic beam. As a consequence, the amplitude of the EXAFS oscillations (Sayers & Bunker, 1988) is attenuated or smeared out, leading to systematic errors in the number of neighbours and Debye–Waller terms. This problem, enhanced for thick samples and for low-energy photons, is difficult to appreciate *a posteriori* and not easily corrected (Goulon *et al.*, 1982; Stern & Kim, 1981).

Owing to the low critical energy of the LNLS storage ring (2.08 keV), third-order harmonic contamination of the Si(111) monochromatic beam is expected to be negligible above the 5 keV range. This might not be the case, however, at the lowest accessible energies of the measurements (down to 2.4 keV). A quantitative evaluation of the harmonic content can be obtained by scanning the monochromator around a fundamental energy (E) and measuring the absorption of a sample with an absorption edge at the energy of the harmonic ($3E$).

In a transmission measurement, α is then obtained from the measured jump and from known values of the linear absorption coefficients (Ramos *et al.*, 1999). We compare the results, with an exponential decay fitted to the data, for the situations before and after August 1999 (Fig. 3). After replacing the windows, the harmonic content has been drastically reduced at low energies. Down to 2800 eV, this contamination can be considered as negligible. This is confirmed through low-energy transmission measurements performed at the Cl K-edge (2820 eV) (Ramos *et al.*, 2001). A standard NaCl powder sample spread onto a tape was measured using an Si(111) monochromator and 1 atm He-filled gas ion chambers with 16 mm of air between them (Fig. 4*a*). It compares very well to harmonic free spectra from the literature (Lytle *et al.*, 1984). Below 2800 eV, the harmonic contamination in transmission measurements starts to be appreciable. At the S K-edge it can be greater than 10%. The distortion at the S K-edge has been experimentally observed by measuring a standard K_2S powder sample spread onto a 50 µm-thick tape. The transmission-mode spectrum presents strong attenuation and distortion compared with CEY results (Fig. 4*b*). In the transmission-mode measurements, the harmonic contamination of the incident beam is enhanced by the absorption of the sample and the support. This effect is eliminated in CEY detection, where all collected electrons come from near the surface of the sample. In CEY detection measurements, the value of α is simply obtained from the ratio of the detected current jump measured by scanning the monochromator around the fundamental energy E and around the energy $3E$, when a sample with an edge at $3E$ is placed inside the detector. The resulting α value around the Cl K-edge has been measured to be smaller than 0.1%, much smaller than the measured value in transmission mode, showing that the harmonic contamination is strongly reduced by using CEY detection.

5. Energy resolution

The energy resolution determines the width of the thinnest measurable feature in an X-ray absorption spectrum. The total energy resolution that can be obtained in an XAS experiment at a chosen

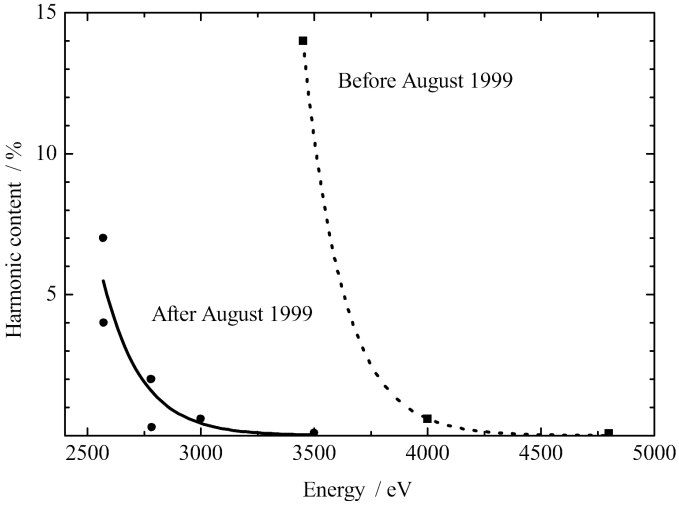

Figure 3
Harmonic contamination in transmission measurements at the XAS beamline, under the normal conditions of measurements: the two ion chambers filled with He and separated by 16 mm of air. The contamination ratios before and after windows substitution are compared.

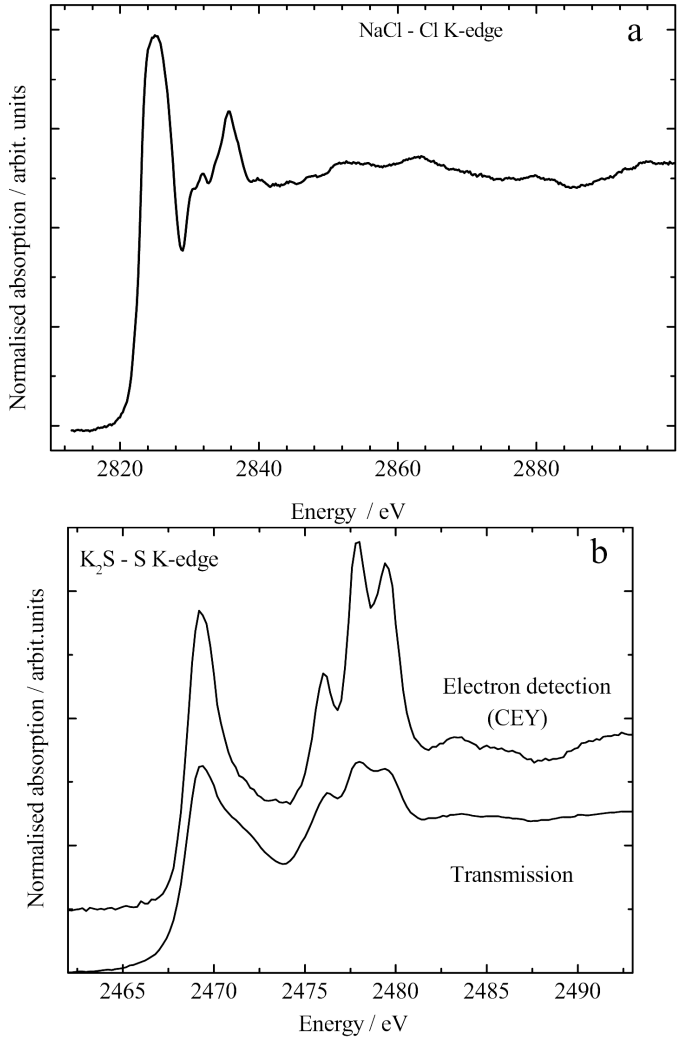

Figure 4
(*a*) Transmission-mode Cl K-edge (2822 eV) XANES spectrum of a standard NaCl powder sample. (*b*) S K-edge XANES in transmission mode compared with conversion electron yield (CEY) mode. Attenuation on the transmission-mode spectrum is due to harmonic contamination.

absorption edge is limited, intrinsically, by the natural width of the core level, Γ (Krause & Oliver, 1979), and, instrumentally, by the X-ray beamline optics. In a simplified scheme for an energy-resolution calculation, each contribution can be considered as having a Gaussian distribution. The resulting overall resolution is simply given by

$$\Delta E_{\rm total} = \left[\Gamma^2 + \sum_i (\Delta E_i)^2\right]^{1/2},$$

where ΔE_i are the relevant instrumental terms: the intrinsic energy resolution of the monochromator, $\Delta E_{\rm mono}$, and the divergence of the beam, $\Delta E_{\rm div}$. The intrinsic energy resolution $[(\Delta E/E)_{\rm mono}]$ depends on the reflection. It is equal to 13.1×10^{-5} for Si(111) and 5.37×10^{-5} for Si(220). The photon beam divergence, $\Delta\theta$, is simply given by $\Delta\theta = (f + s_y)/D$, where f is the vertical slits aperture at a distance D from the source and s_y is the vertical source size. The energy resolution is related to the divergence through $(\Delta E/E)_{\rm div} = \Delta\theta/\tan\theta_{\rm B}$, derived from Bragg's law. As mentioned before, the LNLS storage ring can operate in a normal mode (vertical coupling 0.3%) or in a large beam mode (vertical coupling 3%). We discuss here only the normal mode operation. A complete discussion on energy resolution has been given elsewhere (Ramos *et al.*, 2000). The expected instrumental resolution, for both monochromators used in the XAS beamline and for different slit apertures, is compared with the core-hole contribution (Fig. 5). It can be seen that for the Si(111) monochromator at rather low energies (<6 keV) the instrumental contribution is of the same order as the *K*-shell core hole, but for higher energies the instrumental term starts to dominate, even for a rather small slit aperture. The L_3-edge core-hole width dominates the total energy resolution over almost the whole energy region. For Si(220) the situation is similar, for the range above 10 keV. This monochromator can be used for lower energies when a better energy resolution, compared with Si(111), is needed.

A good evaluation of the energy resolution and its dependence on the slit aperture can be obtained by looking at the FWHM of the very sharp feature at the Mn *K*-edge of $KMnO_4$ (Fig. 6). It represents the transition of a 1*s* electron to the projected 3*d* quasi-localized states into the *p* bands, due to the mixing of the 3*d* and 4*p* orbitals in the tetrahedral symmetry. The measured FWHM for a 0.6 mm slit aperture was ∼2 eV. The ultimate FWHM in this case would be ∼1.5 eV, due to the convolution of the core-hole width (1.16 eV) and the width of the 3*d* band (∼1 eV). The measured FWHM, for different slit apertures, has been deconvoluted by the intrinsic value of 1.5 eV and compared with the expected value for the normal source (continuous line) instrumental resolution (insert of Fig. 6). A good agreement has been observed. For the sake of comparison, the expected value for the large source is also plotted (dashed line). The improvement on the energy resolution is clear when working with the normal source size (s_y = 0.168 mm). Nevertheless, even for null slit aperture, the instrumental contribution to the resolution remains the major term. To eradicate this contribution, one has to use higher-order reflections or the four-reflections monochromator (Tolentino *et al.*, 1995), reducing in that way the contribution of either the intrinsic reflection width or the divergence term.

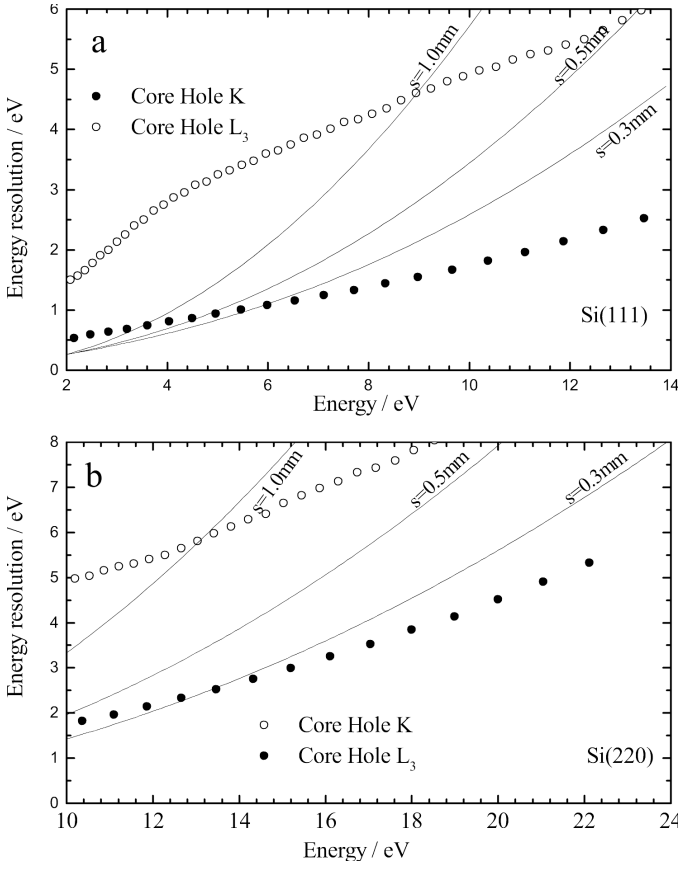

Figure 5
Calculated instrumental energy resolution for the normal source compared with the natural width of the *K* and L_3 core levels for three different slits apertures: (*a*) Si(111) and (*b*) Si(220) crystal monochromators.

6. Energy stability

The search to enhance the signal-to-noise ratio in an XAS spectrum is a crucial concern, especially when one is tracking chemical shifts and

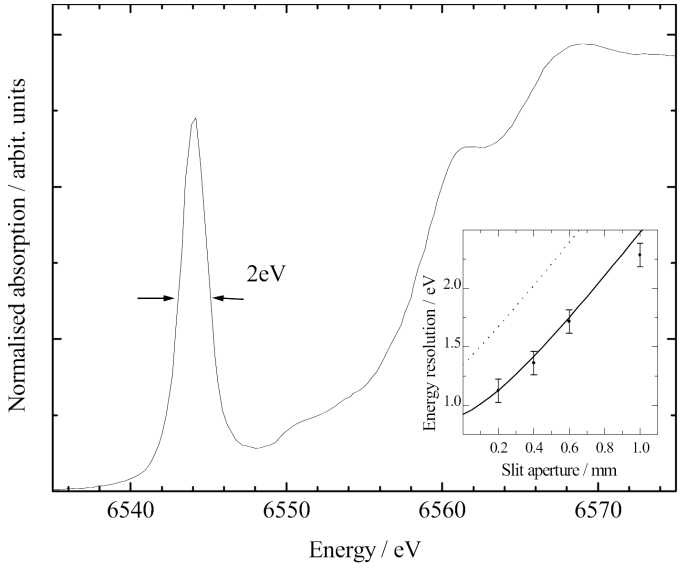

Figure 6
Evaluation of the energy resolution at the Mn *K*-edge. The experimental values are obtained from the FWHM of the pre-edge structure of a $KMnO_4$ powder sample. The FWHM of the pre-peak is ∼2 eV for a slit aperture of 0.6 mm. The comparison of the calculated and measured instrumental energy resolution as a function of the slit aperture is shown in the insert for the normal source (continuous line) and large source (dotted line). The measured points are obtained by deconvolution from core-hole and 3*d*-band width contributions (∼1.5 eV).

seeking tiny variations close to the edge (Fontaine *et al.*, 1992). Most of the differences close to the edge are proportional, directly or indirectly, to the derivative of the edge jump and, very often, the noise and error bars originate from a poor knowledge of the exact energy. Shifts in the energy scale can produce large differences between successive spectra in the XANES region.

The energy scale fluctuation $\Delta E/E$ (or $\Delta\lambda/\lambda$) is directly related to angular ($\Delta\theta/\tan\theta$) and cell-parameters ($\Delta d/d$) fluctuations through Bragg's law. The latter originate uniquely from thermal fluctuations on the Bragg crystal. The former, related to the incidence angle of the photon beam on the crystal, originate from vertical beam source fluctuations and monochromator instabilities.

To obtain an evaluation of the effect of each of these sources of instability, the metallic Co *K*-edge (at 7709 eV) was studied. The energy scale was tracked for three days by looking at the inflection point of the edge-rising jump (Fig. 7). Over successive shifts, the energy-scale repeatability was maintained, considering the same hour of the day, within 0.4 eV. The observed drift during a shift was about 40 meV h^{-1}. Considering that an XANES scan takes about 15 min, one has to consider a drift of about 10 meV between successive scans.

Putting this fluctuation in terms of lattice-parameter variation ($\Delta d/d \simeq 1.3 \times 10^{-6}$), it is equivalent to a temperature variation on the crystal of about 0.5 K, using a value for the silicon thermal expansion coefficient at room temperature of 2.5×10^{-6} K^{-1}. Such temperature stability is not easy to achieve over a period of hours because our channel-cut crystal is not temperature controlled and, also, due to the decay of the photon-beam intensity over the whole day. Fortunately, the total power on the Bragg crystal is very small (1 W at 100 mA, at most, but normally less than 0.1 W) and what happens, in fact, is that the crystal very rapidly reaches stabilization with a slowly monotonously temperature decrease over the day. In Fig. 7, one may observe that the very first points, just after injection of the beam, show the strongest drift.

In terms of angular variation, a 10 meV fluctuation is equivalent to $\delta\theta \simeq 0.34$ µrad. Considering that the source and entrance slits are 10.4 m apart, this is equivalent to a vertical fluctuation of 3.5 µm. As mentioned before, recent changes in the orbit measurement and correction system have improved the vertical-beam-position repeatability between shifts to ±3 µm and orbit fluctuations along a users shift to ±5 µm inside the vacuum chamber (Franco *et al.*, 1999). These figures are compatible with the observed energy-scale fluctuation.

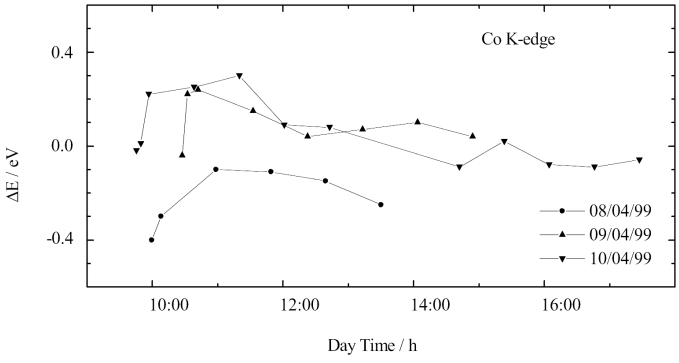

Figure 7
The energy scale at the metallic Co *K*-edge (7709 eV) tracked over three days by looking at the inflection point of the edge-rising jump. Over successive shifts and at the same time of day, the energy-scale repeatability was kept to within 400 meV. The drift along a shift is about 40 meV h^{-1}.

Nevertheless, the vertical fluctuation may be produced either by electron-beam fluctuations or by relative changes in height of the supports of the bending magnet and the entrance slits. In order to keep both elements at the same height (at 1.4 m from the ground) within 3.5 µm, the temperature gradient among both supports should be less than 0.2 K, which is not an easy task. The daily experimental hall variation has been kept within ±2 K. Fortunately, the experimental hall warms up during the day and cools down during the night in a monotonous way, and that should induce a slowly varying drift in the energy scale.

Finally, the last source contributing to the energy-scale fluctuation is a change in length of the thin steel wire that connects the translator stage to the drum of the goniometer (l = 400 mm). A 10 meV (or 0.34 µrad) fluctuation corresponds to a 0.034 µm fluctuation in the wire length (translation stage support) which can be caused by a temperature variation of about 0.7 K. This is also a very critical point and, for that reason, the whole monochromator chamber has been stabilized at a temperature of 301.0 ± 0.2 K.

Considering all these sources of instability, the energy scale has to be monitored by collecting, simultaneously with the spectrum of interest, a spectrum of a reference compound. At the LNLS XAS beamline, a third ion chamber is used in transmission-mode measurements. In decay-mode detection, part of the beam is laterally selected and the fluorescence from a reference standard is collected using a photon counter. In any situation during an XANES measurement, this has proven to be sufficient to solve the problem of the energy-scale fluctuation.

One of the most demanding experiments in terms of energy-scale stability at the LNLS XAS beamline concerns an XMCD experiment (Garcia *et al.*, 2000). The Co *K*-edge XMCD signal of a pure cobalt sample, almost saturated by an applied magnetic field of 0.9 T and for 50% of circularly polarized light, is about 1.6×10^{-3} of the total jump. On the other hand, the derivative of the normalized Co *K*-edge spectrum at the edge is equal to $\delta\mu x/\delta E \simeq 0.1$ eV^{-1} (Fig. 8*a*). This means that an energy-scale fluctuation of $\delta E \simeq 10$ meV generates a signal of the order of 10^{-3} of the total jump. Thence, the figure of 10 meV shift between successive spectra is not good enough for an XMCD measurement. In that case, our data-collection strategy is to select the circularly polarized photons, above or below the plane of the orbit, and to measure the result of four successive measurements ($\Delta\mu^+ = \mu^+ - \mu^- - \mu^- + \mu^+$) at each energy point. μ^+ and μ^- represent each magnetic field orientation, parallel or anti-parallel to the propagation of the beam. Just after, the measurement is repeated starting with another orientation ($\Delta\mu^- = \mu^- - \mu^+ - \mu^+ + \mu^-$). One can observe that, even by collecting the signal point-by-point, a derivative-like signal shows up (Fig. 8*b*). Nevertheless, the real XMCD signal, coming from the difference $\Delta\mu_{\rm XMCD} = \Delta\mu^+ - \Delta\mu^-$, is recovered. The remaining derivative-like signal cancels out, showing that the assumption of a monotonous variation of the energy scale is correct.

7. Summary and conclusions

The LNLS XAS beamline covers a wide energy range, starting at energies as low as 2.3 keV and going up to 25 keV, using Si(111) and Si(220) channel-cut crystal monochromators. The available photon flux in a typical experiment is within the range 10^{10} photons s^{-1} for low and intermediate energies and within the range 10^6–10^7 photons s^{-1} for high energies. Substitution of the windows along the beam path has reduced drastically the harmonic contamination, enabling experiments to be carried out at the S *K*-edge energy. The characterization of the beamline sources of instabilities and upgrades on

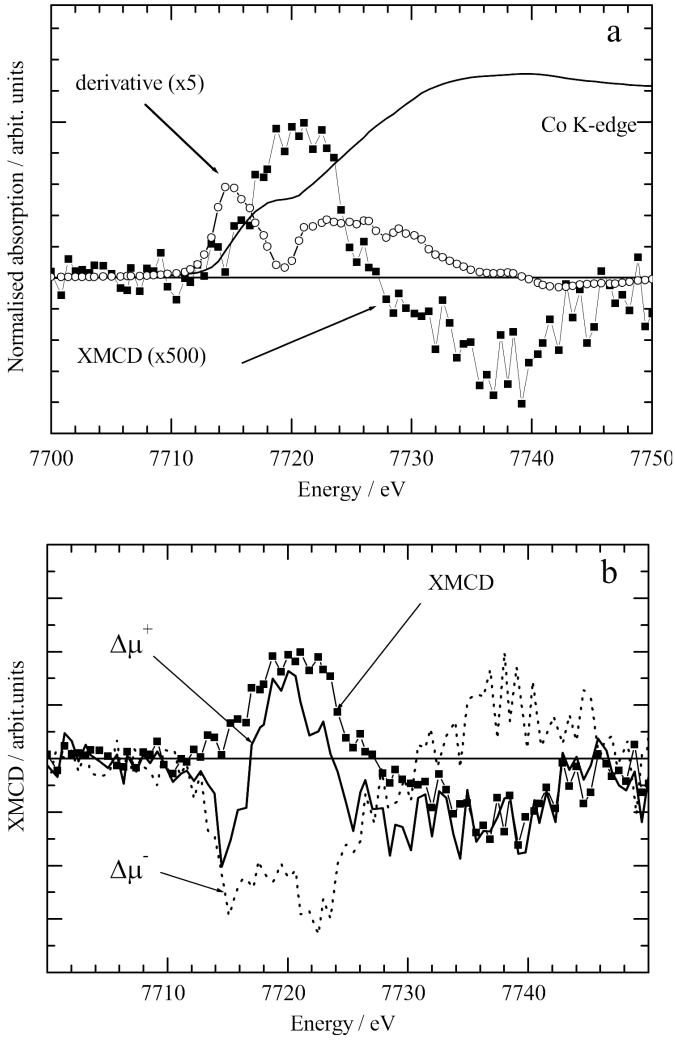

Figure 8
(*a*) Normalized Co *K*-edge spectrum and its derivative, which is equal, at the edge, to $\delta\mu x/\delta E \simeq 0.1\ \mathrm{eV}^{-1}$. An energy scale fluctuation of $\delta E \simeq 10$ meV generates a signal of the order of 10^{-3} of the total jump, comparable with a typical XMCD signal. (*b*) Data-collection strategy: one measures the result of four successive measurements ($\Delta\mu^+ = \mu^+ - \mu^- - \mu^- + \mu^+$) at each energy point ($\mu^+$ and μ^- represent each magnetic field orientation, parallel or anti-parallel to the propagation of the beam), then repeats the measurement, starting with opposite orientation ($\Delta\mu^- = \mu^- - \mu^+ - \mu^+ + \mu^-$), and finally takes the XMCD signal as the difference $\Delta\mu_{\mathrm{XMCD}} = \Delta\mu^+ - \Delta\mu^-$. Even when collecting the XMCD signal point-by-point, a derivative-like signal shows up in each orientation.

electron beam control on the storage ring have helped to improve the stability on the energy scale. The beamline optics and source dimensions are compatible with energy-resolution requirements close to the edges.

The beamline has proved to be a very simple, flexible and confident set-up, covering a wide range of applications. Open to the whole scientific community since July 1997, it has been used by an increasing number of researchers from Brazil and many other countries.

The XAS beamline has been supported by LNLS. We are indebted to the LNLS accelerator physics staff for its assistance and for fruitful discussions. We acknowledge FAPESP for grants and financial support (Proc. No. 95/06439-4, 97/06967-6, 98/16329-0; 99/02688-0; 99/07872-4) and CLAF/CNPq for a grant (Proc. No. 150115/1999-7).

References

Abbate, M., Vicentin, F. C., Compagnon-Cailhol, V., Rocha, M. C. & Tolentino, H. (1999). *J. Synchrotron Rad.* **6**, 964–972.
Alves, M. C. M., Watanabe, N., Ramos, A. Y. & Tolentino, H. (2001). *J. Synchrotron Rad.* **8**, 517–519.
Barbosa, A. F., Guedes, G. P., Tamura, E., Pepe, I. M. & Oliveira, N. B. (1998). *J. Synchrotron Rad.* **5**, 860–862.
Barrea, R. A., Tamura, E. & Tolentino, H. (2001). *J. Synchrotron Rad.* **8**, 381–383.
Craievich, A. F. & Rodrigues, A. R. D. (1998). *Hyperfine Interact.* **113**, 465–475.
Fontaine, A., Baudelet, F., Dartyge, E., Guay, D., Itié, J. P., Polian, A., Tolentino, H. & Tourillon, G. (1992). *Rev. Sci. Instrum.* **63**, 960–965.
Franco, J. G. S., Jahnel, L., Liu Lin, Scorzato, C. & Tavares, P. F. (1999). *Proceedings of the Particle Accelerator Conference*, New York, pp. 2421–2423. Piscataway, NJ: IEEE.
Garcia, F., Sampaio, L. C., Takeuchi, A. Y., Tolentino, H. & Fontaine, A. (2000). *J. Appl. Phys.* **87**, 5881–5883.
Goulon, J., Goulon-Ginet, C., Cortes, R. & Dubois, J. M. (1982). *J. Phys.* **43**, 539–548.
James, R. W. (1982). *The Optical Principles of the Diffraction of X-rays.* Woodbridge, CT: Ox Bow Press.
Krause, M. O. & Oliver, J. H. (1979). *J. Phys. Chem. Ref. Data*, **8**, 329–338.
Lira, A. C., Rodrigues, A. R. D., Rosa, A., Gonçalves da Silva, C. E. T., Pardine, C., Scorzato, C., Wisnivesky, D., Rafael, F., Franco, G. S., Tosin, G., Liu Lin, Jahnel, L., Ferreira, M. J., Tavares, P. F., Farias, R. H. A. & Neuenschwander, R. T. (1998). *Proceedings of the European Particle Accelerator Conference*, Stockholm, Sweden, pp. 626–628. Bristol: Institute of Physics.
Liu Lin, Lira, A. C., Tavares, P. F. & Tosin, G. (1999). *Proceedings of the Particle Accelerator Conference*, New York, pp. 3125–3127. Piscataway, NJ: IEEE.
Lytle, F. W., Greegor, R. B., Sandstrom, D. R., Marques, E. C., Wong, J., Spiro, C. L., Huffman, G. P. & Huggins, F. E. (1984). *Nucl. Instrum. Methods*, **226**, 542–548.
Ramos, A. Y., Tolentino, H. & Alves, M. C. M. (2000). LNLS Technical Memorando Met-01/00. LNLS CP6192 CEP13083-970 Campinas/SP, Brazil.
Ramos, A. Y., Tolentino, H., Alves, M. C. M., Grisolía-Cardona, M., Watanabe, N., Alves, O. L. & Barbosa, L. C. (2001). *J. Mater. Res.* In the press.
Ramos, A. Y., Tolentino, H., Barrea, R. A. & Alves, M. C. M. (1999). LNLS Technical Memorando Met-01/99. LNLS CP6192 CEP13083-970 Campinas/SP, Brazil.
Rodrigues, A. R. D., Craievich, A. F. & Gonçalves da Silva, C. E. T. (1998). *J. Synchrotron Rad.* **5**, 1157–1161.
Sayers, D. E. & Bunker, B. A. (1988). *X-ray Absorption: Principles, Applications, Techniques of EXAFS, SEXAFS and XANES*, edited by D. C. Koningsberger & R. Prins, pp. 211–253. New York: John Wiley.
Stern, E. A. & Kim, K. (1981). *Phys. Rev. B*, **23**, 3781–3787.
Tolentino, H., Cezar, J. C., Compagnon-Cailhol, V., Tamura, E. & Martins Alves, M. C. (1998). *J. Synchrotron Rad.* **5**, 521–523.
Tolentino, H., Durr, J., Mazzaro, I., Udron, D. & Cusatis, C. (1995). *Rev. Sci. Instrum.* **66**, 1806–1808.
Tourillon, G., Dartyge, E., Fontaine, A., Lemonnier, M. & Bartol, F. (1987). *Phys. Lett. A*, **121,** 251–257.